A consistent full-field integrated DIC framework for HR-EBSD

Please check the document version of this publication:

• A submitted manuscript is the version of the article upon submission and before peer-review. There can be important differences between the submitted version and the official published version of record. People interested in the research are advised to contact the author for the final version of the publication, or visit the DOI to the publisher's website.
• The final author version and the galley proof are versions of the publication after peer review.
• The final published version features the final layout of the paper including the volume, issue and page numbers.

Link to publication

A consistent full-field integrated DIC framework for HR-EBSD

T. Vermeij[a], J.P.M. Hoefnagels*[a]

[a]*Dept. Mechanical Engineering, Eindhoven University of Technology, the Netherlands*

Abstract

A general, transparent, finite-strain Integrated Digital Image Correlation (IDIC) framework for high angular resolution EBSD (HR-EBSD) is proposed, and implemented through a rigorous derivation of the optimization scheme starting from the fundamental brightness conservation equation in combination with a clear geometric model of the Electron BackScatter Pattern (EBSP) formation. This results in a direct one-step correlation of the full field-of-view of EBSPs, which is validated here on dynamically simulated patterns. Strain and rotation component errors are, on average, (well) below 10^{-5} for small ($E_{eq} = 0.05\%$) and medium ($E_{eq} = 0.2\%$) strain, and below $3 \cdot 10^{-5}$ for large strain ($E_{eq} = 1\%$), all for large rotations up to $10°$ and 2% image noise. High robustness against poor initial guesses ($1°$ misorientation and zero strain) and typical convergence in 5 iterations is consistently observed for, respectively, image noise up to 20% and 5%. This high accuracy and robustness rivals, when comparing validation on dynamically simulated patterns, the most accurate HR-EBSD algorithms currently available which combine sophisticated filtering and remapping strategies with an indirect two-step correlation approach of local subset ROIs. The proposed general IDIC/HR-EBSD framework lays the foundation for future extensions towards more accurate EBSP formation models or even absolute HR-EBSD.
    https://doi.org/10.1016/j.ultramic.2018.05.001

Keywords: HR-EBSD, Integrated DIC, finite-strain formulation, virtual experiments, high strain accuracy, high angular resolution EBSD, electron backscatter diffraction

1. Introduction

Over the years, Electron Backscatter Diffraction (EBSD) has evolved into a mature technique which is now routinely used to analyze polycrystalline materials at the micron scale [1]. More specifically, Troost et. al. [2] and Wilkinson et.
5 al. [3, 4] introduced the high angular resolution EBSD (HR-EBSD) method to

---

acquire relative elastic strains from the Electron Backscatter Patterns (EBSPs), which can now be readily performed through commercial software packages. Examples of applications include mapping of residual elastic stresses [5, 6], monitoring elastic strains during or after experiments [7, 8, 9, 10] and assessing geometrically necessary dislocation (GND) densities with high sensitivity [11].

As a basic principle of the current *relative* HR-EBSD algorithms, two EBSPs are first filtered (typically with a low and high pass filter in frequency domain [12]) and subsequently compared to acquire the relative deviatoric elastic strain tensor by deriving the deformation gradient tensor from measured shifts of subset regions of interest (ROIs) between the patterns. Following this approach, strain accuracies have been shown to be below 10^{-4} [13]. However, when rotations between patterns exceed ∼0.6°, a finite strain framework must be used in which remapping of the patterns is required to keep the errors to a minimum [14, 15]. Alternatively, *absolute* HR-EBSD analysis may be performed by means of 3D hough transforms [16] or simulation-based HR-EBSD procedures [17, 18, 19], although the same level of accuracy has not yet been reached. The calibration of the EBSD detectors in terms of pattern center (*pc*) and distortions appears to be critical, especially for the absolute HR-EBSD methods [20, 21, 22, 23]. While these works cover powerful methods for elastic strain measurements, all are based on the use of the correlation of subset ROIs (except for unpublished work by Maurice et. al. [24] and the 3D hough transform methods [16]).

In the field of experimental mechanics, correlation of images based on subset ROIs is referred to as 'local' digital image correlation (DIC). An alternative approach was later introduced which is called 'global' DIC, wherein the full image (without the edge region) is correlated in a single optimization routine, which has advantages in terms of accuracy and robustness [25, 26]. In addition, the continuous increase in computational power has given rise to novel parameter identification methods such as finite element model updating (FEMU) [27] and integrated digital image correlation (IDIC) [28, 29, 30], which both use a (mechanical) model at the background. FEMU uses a two-step approach where mechanical parameters are optimized by comparing displacement (or strain) fields acquired from experimental images (using standard, *local* DIC) to the displacements (or strains) from a FE simulation. Instead, in IDIC, images are directly correlated, in a one-step approach, by optimization of the mechanical parameters (and/or e.g. parameters involved in SEM artifacts [31]) that govern the (material) deformation observed in the images. Interestingly, while FEMU and IDIC are based on a similar mathematical formulation, comparison of the methods show that IDIC produces less erroneous and more reliable results than FEMU, particularly for more challenging test cases exhibiting small displacements, complex kinematics, misalignment of the specimens, and image noise [32]. Arguably, the current HR-EBSD techniques can be considered as FEMU-type algorithms, because shifts (displacements) are first correlated using *local* DIC after which an optimization algorithm is used to acquire the rotation and strain components. Note, however, that these FEMU-type algorithms have been amended with sophisticated image processing strategies such as remapping and

low and high pass filtering.

Therefore, the aim of this rapid communication is to present a robust, transparent IDIC algorithm for high angular resolution EBSD, by means of a rigorous linearization of the non-linear bright conservation equation in a consistent mathematical framework, based on a clear geometric model of the EBSP formation, without the need for remapping or filtering. To elucidate all assumptions in the IDIC algorithm, its derivation will start from the basis of all DIC algorithms, i.e. brightness conservation, into which the geometric EBSP model is introduced. To validate this IDIC/HR-EBSD framework, virtual experiments are performed by correlating dynamically simulated EBSPs with relatively large deformations of up to 1% equivalent strain combined with large rotations of up to 10° and in combination with significant image noise of 2%. We will show that strain components can be robustly identified with errors in the order of 10^{-5} under these challenging conditions.

2. Methodology

2.1. Derivation of a consistent IDIC framework for HR-EBSD

The derivation of the framework starts by assuming that the captured images (EBSPs) contain brightness features that follow a certain displacement field (in the detector screen plane). In other words, it is assumed that the brightness of the projection of a crystal direction $[hkl]$ onto the detector is constant in all acquired EBSPs, although this brightness conservation can be relaxed to incorporate background profiles typically observed in experimental EBSPs. In the derivation that follows, we aim to exploit the brightness conservation by allowing the incorporation of a model of the EBSP formation, which can depend on a number of physical parameters such as strain and rotation components. Following the rigorous derivation of the IDIC framework [33], the brightness conservation is formulated as follows:

$$r(\vec{x_0}, \{\lambda\}) = f(\vec{x_0}) - g(\vec{x}(\vec{x_0}, \{\lambda\})), \text{ with } \vec{x}(\vec{x_0}, \{\lambda\}) = \vec{x_0} + \vec{u}(\vec{x_0}, \{\lambda\}), \quad (1)$$

where $f(\vec{x_0})$ is the reference pattern (with $\vec{x_0}$ constituting the original pixel locations) and $g(\vec{x}(\vec{x_0}, \{\lambda\}))$ the deformed pattern (with $\vec{x}$ denoting the deformed coordinates). The residual $r(\vec{x_0}, \{\lambda\})$ will reduce to the acquisition noise if the approximated displacement field $\vec{u}(\vec{x_0}, \{\lambda\})$, in de detector plane, is correct. To remedy the ill-posedness inherent to DIC [30, 32], this field is regularized with a set of n unknown degrees of freedom (DOFs) $\{\lambda\} = [\lambda_1, \lambda_2, \lambda_i, ..., \lambda_n]^t$ (e.g. strain and rotation components), each associated to certain shape functions $\vec{\phi_i}$, as discussed below. The solution $\{\lambda\}$ is retrieved from the minimization of the quadratic residual norm, Ψ,

$$\{\lambda\} = \underset{\lambda}{\text{Argmin }} \Psi(\{\lambda\}), \text{ with } \Psi(\{\lambda\}) = \int_\Omega [r(\vec{x_0}, \{\lambda\})]^2 \, d\vec{x}, \quad (2)$$

in which Argmin denotes the minimization with respect to the DOFs $\{\lambda\}$ and Ω is the global region of interest (gROI) over which the residual is minimized.

3

The solution for the optimal DOFs is a non-linear problem, which is linearized and solved for iteratively with a modified Newton-Raphson scheme, for which the consistent derivation of the one-step linearization is given in detail in [33]. The linearized system of equation is written in matrix form as

$$[\mathbf{M}]\delta\{\lambda\} = \{\mathbf{b}\}, \tag{3}$$

in which $\delta\{\lambda\}$ is the iterative update of the DOFs, i.e. $\{\lambda\}^{(k+1)} = \{\lambda\}^{(k)} + \delta\{\lambda\}$, where $\{\lambda\}^{(k)}$ is initialized with the initial guess $\{\lambda\}_0$. Components of the DIC matrix $[\mathbf{M}]$ and the right hand side member $\{\mathbf{b}\}$ read

$$M_{ij} = \int_\Omega \left((\vec{\nabla} g \cdot \vec{\phi}_i)(\vec{\nabla} g \cdot \vec{\phi}_j) \right) \, d\vec{x}, \tag{4}$$

$$b_j = \int_\Omega \left((\vec{\nabla} g \cdot \vec{\phi}_j) r \right) \, d\vec{x}, \tag{5}$$

where the image gradient $\vec{\nabla} g(\vec{x})$ is used, because it was shown in [33] that this image gradient achieves good initial guess robustness under conditions of large rotations. The basis functions $\vec{\phi}_i$ are defined as

$$\vec{\phi}_i (\vec{x_0}, \{\lambda\}) = \frac{\partial \vec{u}(\vec{x_0}, \{\lambda\})}{\partial \lambda_i}. \tag{6}$$

These partial derivatives of the displacement field, with respect to the DOFs, represent the sensitivity fields to a change in the corresponding DOF. The geometric EBSP formation model, which is defined hereafter, enters the optimization routine through the choice of the displacement field as a function of the DOFs, i.e. $\vec{u}(\vec{x_0}, \{\lambda\})$. With this, all ingredients necessary to solve for the update of the DOFs are in place. The derived iterative procedure is run until convergence is met. In this work, the convergence criterion is based on the L^2-norm of the right hand side member [30], with a low value of

$$||\{\mathbf{b}\}|| < 10^{-6}. \tag{7}$$

2.2. Geometric EBSP formation model for HR-EBSD

To acquire the displacement field

$$\vec{u}(\vec{x_0}, \{\lambda\}) = \vec{x}(\vec{x_0}, \{\lambda\}) - \vec{x_0}, \tag{8}$$

a model for the position vector of each pixel in the deformed pattern must be derived. Figure 1 shows two different views of the geometry and kinematics of a reference and deformed EBSP which contains all relevant vectors to derive $\vec{x}(\vec{x_0}, \{\lambda\})$, and thus also $\vec{u}(\vec{x_0}, \{\lambda\})$. The undeformed EBSP f contains pixels associated to position vectors (in the detector plane) $\vec{x_0}$, which can also be formulated in 3D with the specimen source point as origin

$$\vec{x_0}'' = dd_0 \vec{e_z} + \vec{x_0}', \quad \text{with} \quad \vec{x_0}' = \vec{x_0} - \vec{x_0}^{pc}, \tag{9}$$

4

where $\vec{x_0''}$ now represents the projection of a crystal direction [hkl] in the reference point onto the detector screen. Subsequently, $\vec{x_0''}$ is transformed by the relative deformation gradient tensor, $\mathbf{F_r}$, working directly between the reference and deformed crystal, into $\vec{x''}$

$$x^{\vec{}''} = \mathbf{F_r} \cdot \vec{x_0''}, \text{ with } \mathbf{F_r} = (\vec{\nabla}_0 \vec{x''})^T, \tag{10}$$

with $\mathbf{F_r}$ defined in the coordinate system of figure 1a. The new (deformed) pixel position is found by projecting $\vec{x''}$ on the detector screen

$$\vec{x'} = \frac{dd}{\vec{e_z} \cdot \vec{x''}} \left(\vec{x''} - (\vec{e_z} \cdot \vec{x''})\vec{e_z} \right), \tag{11}$$

after which the actual position vector is retrieved

$$\vec{x} = \vec{x'} + \vec{x}^{pc}. \tag{12}$$

Then the displacement field is obtained by combination of equations 8-12

$$\vec{u}(\vec{x_0}, \{\lambda\}) = \frac{dd}{\vec{e_z} \cdot \mathbf{F_r} \cdot (dd_0\vec{e_z} + \vec{x_0} - \vec{x_0}^{pc})} \Big(\mathbf{F_r} \cdot (dd_0\vec{e_z} + \vec{x_0} - \vec{x_0}^{pc}) -$$
$$\left(\vec{e_z} \cdot \mathbf{F_r} \cdot (dd_0\vec{e_z} + \vec{x_0} - \vec{x_0}^{pc}))\vec{e_z} \right) + \vec{x}^{pc} - \vec{x_0}. \tag{13}$$

To accommodate the implementation of this geometric model for HR-EBSD into the IDIC framework, the choice is made to use the individual components of the relative deformation gradient tensor $\mathbf{F_r}$ as DOFs. Because the current model is insensitive to the hydrostatic expansion, similar to other state-of-the-art HR-EBSD formulations (e.g. [14, 15]), $F_{r_{33}}$ is formulated in terms of the elastic material constants and all other $\mathbf{F_r}$ components (derived analytically using the Matlab Symbolic Toolbox in advance), according to a plane stress assumption, obtained using basic continuum mechanics:

$$\vec{e_3} \cdot \sigma \cdot \vec{e_3} = 0, \text{ with } \sigma = \frac{1}{det(\mathbf{F_t})} \mathbf{F_t} \cdot \mathbf{S} \cdot \mathbf{F_t}^T, \tag{14}$$

where σ is the Cauchy stress tensor in the sample coordinate system, pulled forward from the second Piola Kirchhoff stress tensor $\mathbf{S}$:

$$\mathbf{S} = {}^4\mathbf{C} : \mathbf{E}, \text{ with } \mathbf{E} = \frac{1}{2}(\mathbf{F_t}^T \cdot \mathbf{F_t} - \mathbf{I}), \tag{15}$$

wherein $\mathbf{E}$ denotes the Green Lagrange strain tensor and $\mathbf{I}$ a unity tensor. Additionally, ${}^4\mathbf{C}$ and $\mathbf{F_t}$ prescribe the fourth order elastic stiffness tensor and the total deformation gradient tensor, respectively, with respect to the non-rotated crystal. All input parameters and results are expressed in the more transparent strain and rotation components, which are directly related to $\mathbf{F_r}$ at all times. The strain definition used here is the symmetric Green Lagrange strain tensor $\mathbf{E}$

as defined in equation 15, to allow for large rotations and large strains. The rotations are expressed in the following Euler angles (in the Tait-Bryan convention): $\mathbf{R} = X^1 Y^2 Z^3$, with rotation angles θ_x, θ_y and θ_z. Additionally, as a convenient use to express the misorientations, quaternion rotations are used, which consists of a rotation of magnitude θ_q over a unit vector $x_{\theta_q}\vec{e_x} + y_{\theta_q}\vec{e_y} + z_{\theta_q}\vec{e_z}$.

Additionally, it is well known that, in actual EBSPs, the overall contrast and brightness vary over the detector screen [34]. Here, its zero order effect is simply taken into account by including two constant sensitivity fields of value 1, ϕ_{con} and ϕ_{br} (with λ_{con} and λ_{br} their associated DOFS), in the brightness conservation equation [35], yielding a modification of equation 1:

$$r(\vec{x_0}, \{\lambda\}) = f(\vec{x_0}) - g(\vec{x}(\vec{x_0}, \{\lambda\})) + \lambda_{con}\phi_{con}f(\vec{x_0}) + \lambda_{br}\phi_{br}. \qquad (16)$$

The actual inhomogeneous profiles of the contrast and brightness change over the detector screen can easily be added to the framework at a later stage, by changing ϕ_{con} and ϕ_{br} to mimic the real change in contrast and brightness profiles. In this way, the remaining background profile after background division or subtraction can be captured using spatially-varying relaxation fields.

Finally, to take advantage of the full pattern, the location of the gROI is determined with the initial guess DOFs ($\{\lambda\}_0$), where the area of the gROI is taken to be as large as possible (with the exception of a 50 pixel edge region) for an optimal correlation, as will be shown in figure 2.

2.3. Virtual experimentation

To objectively evaluate the performance of the algorithm, virtual experiments have been performed, employing our novel IDIC-based HR-EBSD method on dynamically simulated EBSPs, to assess robustness and accuracy.

To show the generality of the IDIC/HR-EBSD framework, all EBSPs stem from the complex crystal structure 1T' Molybdenum Ditelluride (1T'-MoTe2), which are dynamically simulating in Esprit DynamicS[1] (based on [36]) using appropriate lattice parameters as given in table 1. Separate simulations are performed for three deformed crystals without rotation (denoted by small, medium and large strains), which will each be used as a "reference" pattern, and one undeformed (no strain) crystal which is rotated in various directions to yield the "deformed" patterns. The 8-bit patterns of 1465x1465 pixels are acquired by performing simulations at 70° tilt using a $20keV$ electron beam, with default values for the absorption length ($59\mathring{A}$), excitation depth ($46\mathring{A}$), Debye-Waller-B parameters (0.73 for the crystal and 0.3 for the source), minimum lattice spacing ($0.5\mathring{A}$) at a quality factor of 5. Similar to all current publications on relative HR-EBSD, it is assumed that the pc coordinates and dd are known for each EBSP, therefore, here, the pc coordinates are kept constant at $\vec{x_0}^{pc} = \vec{x}^{pc} = (0.5 \cdot 1465,\ 0.3 \cdot 1465)$ (x and y coordinate, defined from the top-left of the EBSP), while the detector distance is fixed at $dd_0 = dd = 0.5 \cdot 1465$.
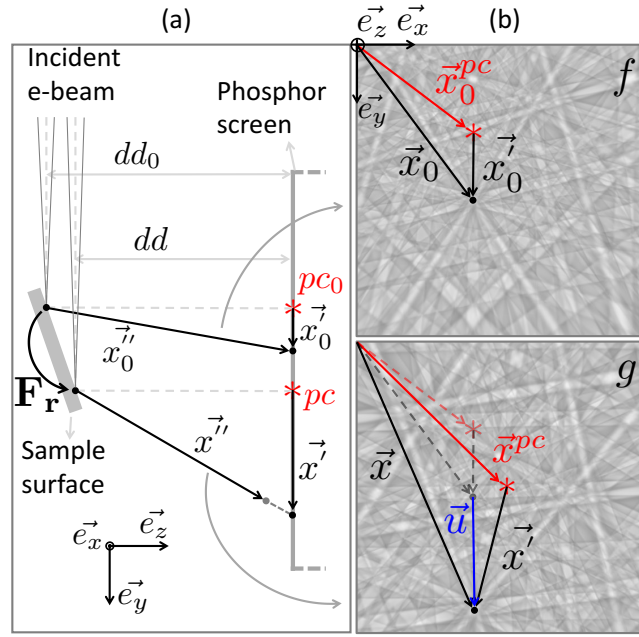
Figure 1: HR-EBSD geometry and kinematics between a reference and deformed EBSP. (a) Sideview showing two source points in the specimen (reference and deformed point, between which a deformation gradient tensor $\mathbf{F_r}$ acts) giving rise to two distinct EBSPs on a detector screen with certain pc locations (red crosses) and detector distances (dd). The position vectors on the detector w.r.t. the sample source point ($\vec{x_0''}$ and $\vec{x''}$) and the pc ($\vec{x_0'}$ and $\vec{x'}$) are depicted. (b) Front views on the detector screen, showing EBSPs from the reference (f) and deformed (g) source points. pc locations ($\vec{x_0}^{pc}$ and $\vec{x}^{pc}$) and in-plane position vectors ($\vec{x_0}$ and $\vec{x}$), all w.r.t. the top-left of the screen, are included, as well as the resulting displacement vector $\vec{u}$ on the detector.

All errors are reported as the absolute error ϵ_α,

$$\epsilon_\alpha = |\alpha - \alpha^{ref}|, \tag{17}$$

where α represents a certain resulting parameter (such as a strain component), while α^{ref} is the value of the same parameter that was used to generate the specific virtual experiment. Considering the (unknown) error in the dynamic simulation of the EBSPs with Esprit DynamicS, ϵ_α yields an upper bound of the real error in α. The strain error ϵ_E denotes the mean of the error of all individual strain components of **E**.

To assess the performance of the framework in a realistic setting, the initial guesses of the DOFs always deviate from the reference parameter used to perform the virtual experiments. To this end, the relative strain between two patterns is assumed to be zero (**E** = 0) at the start of a correlation, while the initial guess rotation parameters are chosen such that there is always a minimum error in quaternion angle of 1° between the patterns, which is well above the maximum error in the rotation measured with commercial EBSD packages based on the Hough transform [37]. A unique random noise is also added to each pattern, albeit the exact nature of camera noise is non trivial (e.g. heteroscedastic [38]) and highly dependent on the type of camera sensor, e.g. CCD versus CMOS, the details of which is not the purpose of this study. Therefore, here, we follow the bulk of DIC literature and add a simple Gaussian white noise to the patterns, with the standard deviation defined as a percentage of the root mean square of the EBSP intensity.

We present two case-studies in which we evaluate robustness and accuracy. First, a set of two patterns is correlated with a focus on the robustness to noise and erroneous initial guesses, where we also present the functioning of the framework in more detail. Finally, we will evaluate the accuracy of the algorithm at several levels of complex strain over a range of rotations.

Table 1: Applied strains and corresponding lattice parameters used for the dynamic simulation of EBSPs

	No strain	Small strain	Medium strain	Large strain
E_{eq}	**0**	**$5 \cdot 10^{-4}$**	**$2 \cdot 10^{-3}$**	**$1 \cdot 10^{-2}$**
E_{11}	0	$3 \cdot 10^{-4}$	$1.2 \cdot 10^{-3}$	$-7.5 \cdot 10^{-3}$
E_{22}	0	$2 \cdot 10^{-4}$	$-8 \cdot 10^{-4}$	$3 \cdot 10^{-3}$
E_{33}	0	$-2.1 \cdot 10^{-4}$	$-1.7 \cdot 10^{-4}$	$1.9 \cdot 10^{-3}$
E_{12}	0	$1.5 \cdot 10^{-4}$	$-5 \cdot 10^{-4}$	0
a $[\mathring{A}]$	6.33	6.33190	6.33759	6.28235
b $[\mathring{A}]$	6.33	6.33127	6.32493	6.34897
c $[\mathring{A}]$	6.33	6.32864	6.32891	6.34220
γ $[°]$	90	90.0171	89.9427	90

8

3. Results and discussion

Figure 2 summarizes the correlation between a reference undeformed pattern f and a *medium* (c.f. table 1) deformed pattern g (both with 2% random gaussian noise) which is also rotated by 10°. Figure 2a and b show the undeformed and deformed EBSP with their associated maximized gROIs between which the correlation is performed. Figure 2c illustrates the image residual at the initial guess (which has no deformation and 1° error in quaternion rotation), where the Kikuchi bands can still be clearly seen, mainly because of negative and positive peaks at the band edges, indicating that the values of the DOFs are incorrect. Subsequent minimization of the image residual typically results in convergence in 5 iterations as shown in figure 2d. We estimate the computational time of the IDIC/HR-EBSD framework to be approximately 3 times slower than a remapping-assisted cross-correlation based HR-EBSD algorithm (when both are implemented in our inefficient Matlab code.) In 2d, the error of individual deformation gradient tensor components ($\epsilon_{F_{ij}}$) converge to values in the range of $\sim 10^{-6}/10^{-5}$, on this case of dynamically simulated patterns. This correlation results in the image residual (after convergence) depicted in Figure 2e, showing no signs any more of the Kikuchi bands, indicating a successful correlation. The robustness to variations in initial guess parameters is illustrated in figure 2f, where a variation in (initial guess) rotation errors (blue circles) is performed by each time changing all three Euler angles (θ_x, θ_y and θ_z) to either $+1°$ or $-1°$, corresponding to a misorientation in terms of the quaternion angle of $\theta_q = \sim 1.7°$ for all 8 cases, while the initial guess of the strain components are always zero. The errors in rotation after convergence (in red circles) are all below 10^{-5}, as shown in the inset, while the errors in the strain components also converge to values below 10^{-5} (not shown here). This clearly demonstrates the high initial guess robustness of the IDIC-based HR-EBSD routine. Finally, figure 2g presents the robustness to random gaussian noise (10 unique noise profiles were enforced at each level for statistics). To this end, the mean strain error (ϵ_E) is plotted over increasing noise levels reaching 20%, with insets visually showing the noise in EBSPs and residuals. At fairly large noise levels of up to 5%, the strain errors remain relatively small (below 10^{-5}), whereas a further increase of the noise causes lower accuracies, but remarkably still below 10^{-4} for extreme noise of 20% (which is comparably noisy to "Poisson noise level 16" from [39]), though at the expense of an increase in the number of iterations required for proper convergence. Note that, in IDIC, the image residual field is often recommended as a powerful tool to evaluate the performance of the algorithm in experiments and to assess the correlation convergence and possible systematic errors in the underlying model, which can be identified from regions in the residual field with increased amplitude, as, e.g., demonstrated in [40]. Therefore, the residual field is also recommended as a quality metric for the IDIC/HR-EBSD framework, when applied to experimental EBSPs.

In figure 3, errors after correlation of a range of patterns with three levels of complex deformation are explored with varying rotation up to 10° between the patterns, all at noise levels of 2%, where the focus is on strain and rotation
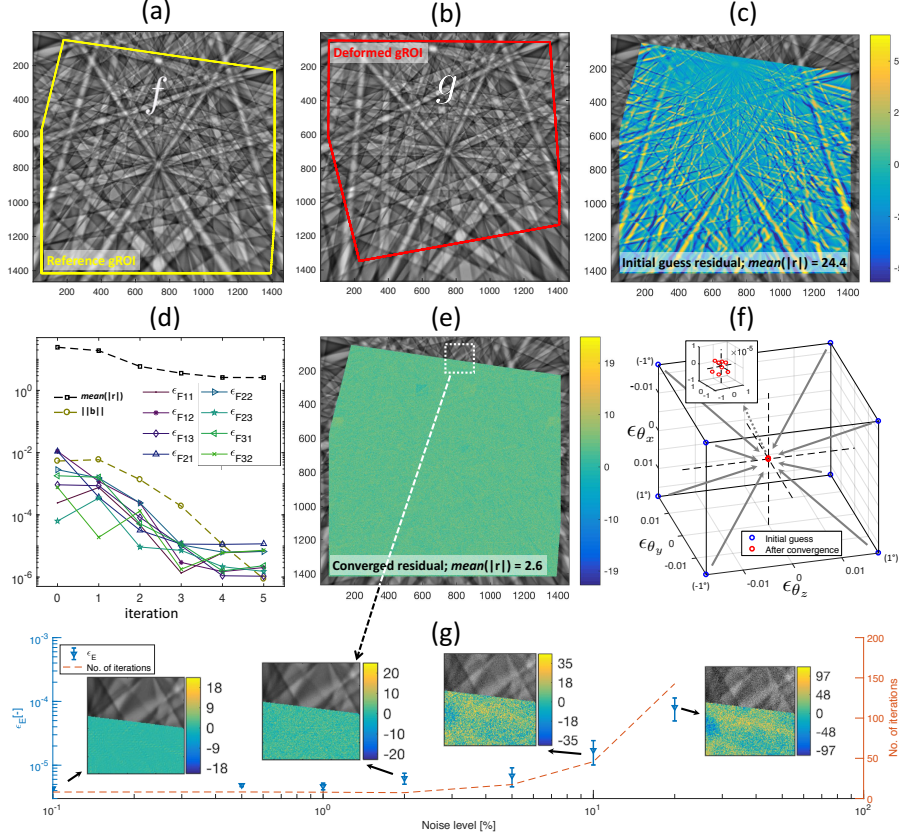
9

Figure 2: **(Full page-width figure preferred)** Correlation case-study and convergence behaviour of a set of 2 patterns with medium deformation (as defined in table 1). (a) Reference EBSP f with optimized gROI. (b) Deformed EBSP g with deformed gROI. (c) Image residual plotted in f at initial guess DOFs $\{\lambda\}_0$. (e) Convergence behaviour, with $mean(|r|)$, $||b||$, and $\epsilon_{F_{ij}}$ at each iteration until convergence is reached. (e) Image residual plotted in f after convergence is met; note the different colorbar ranges. (f) Initial guess robustness: different poor initial guess parameters (all strain components zero and $+1°$ or $-1°$ rotation error for each of the three Euler angles, θ_x, θ_y and θ_z) converge robustly to errors in the rotation below 10^{-5} as shown in the inset, and equally low errors in the strain components (not shown). (a-f) all results at a noise level of 2%. (g) The mean of the strain error and of the number of iterations required for convergence, averaged over 10 noise realizations, plotted as a function of the noise level, where the insets show examples of the EBSPs and image residuals (each with a different colorbar range), of which the locations is given by the white box in (e).

10

accuracy in this case of virtual experimentation. To avoid a possible bias towards
a specific rotation direction, the applied quaternion rotations have three distinct
axes of rotation, as given in the legend of figure 3b, with 10 rotations over each
axis.

The levels of deformation in figures 3a, 3b and 3c correspond to equivalent
green lagrange strains of $E_{eq} = 5 \cdot 10^{-4}$, $E_{eq} = 2 \cdot 10^{-3}$ and $E_{eq} = 1 \cdot 10^{-2}$,
respectively. At each deformation level, no significant trend can be seen in the
errors over increasing rotations, demonstrating that the remapping strategy is
not required for the here-proposed IDIC-based HR-EBSD approach. Interest-
ingly, at both *small* and *medium* strain levels (figure 3a and b), the errors reside
below 10^{-5} (with all of the 6 individual strain component errors below $1.6 \cdot 10^{-5}$
for $\theta_q < 4°$ while all remaining below $2 \cdot 10^{-5}$ for θ_q up to 10°). Yet, the (less
realistic) large deformation of 1%, as shown in figure 3c, shows increased errors
approaching $3 \cdot 10^{-5}$ (with the 6 errors of individual strain components of **E** all
below $6 \cdot 10^{-5}$), which again remain approximately constant over the increasing
quaternion rotation. Note that the *pc* coordinates, assumed constant through-
out this communication, can easily be varied. Introduction in the correlation
of a known, *relative*, *pc* shift ($\vec{x}^{pc} - \vec{x_0}^{pc}$, $dd - dd_0$), caused by scanning of
the electron beam, does not result in an increase of errors, as confirmed by a
few simple virtual experiments. In experimental analysis, however, it is well
known that an error in the *absolute* location of the pattern center ($\vec{x_0}^{pc}$, dd_0)
introduces large strain errors for *absolute* simulation-based HR-EBSD [20, 22],
while it was also shown to introduce less but still significant errors for *relative*
remapping-based HR-EBSD at large rotations [15]. Preliminary tests for the
IDIC/HR-EBSD framework show similar errors, but this effect should be ex-
plored in detail in the future. Note, also, that (perhaps a large) part of the
errors stems from the way the virtual EBSPs are generated and discretized us-
ing dynamical simulations (with Esprit DynamicS) prior to the IDIC/HR-EBSD
analysis, therefore, the errors in the IDIC/HR-EBSD framework are probably
smaller than the errors reported here.

The low errors in both strain and rotation components, below 10^{-5}, at the
small and *medium* deformations seem to be, respectively, similar to and better
than those reported in Ref. [14] and Ref. [15], where deformed dynamically
simulated patterns with large rotations are correlated using subset ROIs, after
applying advanced filtering and remapping strategies. Note, however, that spe-
cific testing conditions differ, making a direct comparison challenging. At larger
elastic strain up to 1%, the correlation is still very accurate; this high level of
deformation has so far remained rather unexplored in *relative* HR-EBSD, which
prevents direct comparison to the literature, although several attempts have
been done using *absolute* simulation based HR-EBSD [18]. We hypothesize that
the increase in error at 1% elastic strain originates from a combination of effects:
the widening of Kikuchi bands and the movement of individual bands. These
second order effects contradict the assumption of a homogenous deformation
between patterns (as implied by the constant deformation gradient tensor), and
thus can act as sources of error. Additionally, uncertainties in the knowledge
of absolute crystal rotation and elastic stiffness constants will introduce errors

11

Figure 3: Strain and rotation errors plotted over a range of deformed (dynamically simulated) EBSPs with increasing quaternion angles up to $10°$ at (a) $5 \cdot 10^{-4}$, (b) $2 \cdot 10^{-3}$ and (c) $1 \cdot 10^{-2}$ equivalent green lagrange strains (according to table 1), and for three different quarternion axes, which are given in the legend of (b) and marked with different colors. All results from virtual experimentation are obtained for an initial guess of zero strain and $1°$ of quaternion misorientation, and for a noise level of 2%.

in the correlation of the relative strains and rotations, which is expected for all HR-EBSD algorithms in which the plane stress assumption is utilized. The resulting strain errors are expected to be lower for the one-step correlation of the IDIC framework, conform Ref. [32], although this should be tested in the future.

In the mind of the authors, the robustness and consistency of the proposed IDIC/HR-EBSD framework is essential in guaranteeing high accuracy in experimental analysis. Moreover, this may enable the analysis of more advanced problems such as relative HR-EBSD correlation between different grains, i.e. much larger rotations than shown here. Additionally, the transparent IDIC framework allows implementation of more complex geometric EBSP formation models, e.g. to include the change in Kikuchi band width to determine the hydrostatic strain, to include the so-called 'barrel' distortion due to optical imaging of the EBSP through the phosphor screen onto the CCD detector, or even to include a model for absolute HR-EBSD, without being compromised by dedicated filtering and remapping strategies that are specifically optimized for one particular function. Finally, similar to other IDIC frameworks [41], this IDIC/HR-EBSD framework can easily be set up to correlate multiple images (EBSPs) in a single optimization step, which may give a significant advantage for accurate identification of insensitive parameters that are shared among EBSPs, e.g., to accurately identify and correct for drift between the specimen and the detector or even to perform absolute HR-EBSD. Such possibilities will be explored in the future.

4. Conclusions

A general integrated digital image correlation (IDIC) framework for high angular resolution EBSD (HR-EBSD) has been developed, in a finite strain framework, through a rigorous, consistent linearization of the fundamental brightness conservation equation and by inserting a transparent geometric model of the EBSP formation in the resulting Gauss-Newton optimization scheme. Because the complete field of view (optimized global ROI) is correlated in a single optimization step (compared to the indirect two-step correlation approaches based on local subset ROIs in the literature), high accuracy and robustness are achieved, in virtual experimentation, without the need for advanced filtering and remapping strategies. The following features have been demonstrated:

- The strain and rotation component errors remain, on average, (well) below 10^{-5} for small and medium strain levels of $E_{eq} = 5 \cdot 10^{-4}$ and $E_{eq} = 2 \cdot 10^{-3}$, and below $3 \cdot 10^{-5}$ for large strain of 1%, all for 2% noise in the EBSPs. This high accuracy can match the most accurate, yet more sophisticated relative HR-EBSD algorithms that are currently available in the literature [14, 15], when comparing validation on dynamically simulated patterns.

- High robustness and typical convergence in 5 iterations of the IDIC/HR-EBSD optimization routine is consistently observed for all cases with poor initial guesses of at least 1° quaternion misorientation and zero strains and

13

image noise up to 5%. The convergence remains robust (and accurate) for image noise increasing up to 20% of the dynamic range.

The EBSP formation model provides the in-plane displacement field on the detector as a function of deformation gradient tensor and the geometric properties, such as the pattern center, *pc*. Therefore, by making the EBSP formation model more realistic, the generic IDIC/HR-EBSD framework can readily be extended to include, e.g., Kikuchi band width variations or lens-induced optical distortions.

References

[1] F. J. Humphreys, Review grain and subgrain characterisation by electron backscatter diffraction, Journal of Materials Science 36 (16) (2001) 3833–3854. `doi:10.1023/A:1017973432592`.
URL `https://doi.org/10.1023/A:1017973432592`

[2] K. Troost, P. Van der Sluis, D. Gravesteijn, Microscale elastic-strain determination by backscatter kikuchi diffraction in the scanning electron microscope, Applied Physics Letters 62 (10) (1993) 1110–1112. `doi:10.1063/1.108758`.
URL `https://doi.org/10.1063/1.108758`

[3] A. J. Wilkinson, Measurement of elastic strains and small lattice rotations using electron back scatter diffraction, Ultramicroscopy 62 (4) (1996) 237 – 247. `doi:10.1016/0304-3991(95)00152-2`.
URL `http://www.sciencedirect.com/science/article/pii/0304399195001522`

[4] A. J. Wilkinson, G. Meaden, D. J. Dingley, High-resolution elastic strain measurement from electron backscatter diffraction patterns: New levels of sensitivity, Ultramicroscopy 106 (4-5) (2006) 307–313. `doi:10.1016/j.ultramic.2005.10.001`.
URL `http://linkinghub.elsevier.com/retrieve/pii/S0304399105002251`

[5] M. Kartal, F. Dunne, A. Wilkinson, Determination of the complete microscale residual stress tensor at a subsurface carbide particle in a single-crystal superalloy from free-surface EBSD, Acta Materialia 60 (13-14) (2012) 5300–5310. `doi:10.1016/j.actamat.2012.06.027`.
URL `http://linkinghub.elsevier.com/retrieve/pii/S1359645412003990`

[6] J. Jiang, T. B. Britton, A. J. Wilkinson, Mapping type III intragranular residual stress distributions in deformed copper polycrystals, Acta Materialia 61 (15) (2013) 5895–5904.
URL `http://www.sciencedirect.com/science/article/pii/S1359645413004709`

[7] J. Ast, G. Mohanty, Y. Guo, J. Michler, X. Maeder, In situ micromechanical testing of tungsten micro-cantilevers using HR-EBSD for the assessment of deformation evolution, Materials & Design 117 (2017) 265–266. `doi:10.1016/j.matdes.2016.12.052`.
URL `http://linkinghub.elsevier.com/retrieve/pii/S0264127516315787`

[8] M. J. McLean, W. A. Osborn, In-situ elastic strain mapping during micromechanical testing using ebsd, Ultramicroscopy 185 (Supplement C)

405 (2018) 21 – 26. `doi:10.1016/j.ultramic.2017.11.007`.
URL `http://www.sciencedirect.com/science/article/pii/S0304399117303042`

[9] E. Plancher, J. Petit, C. Maurice, V. Favier, L. Saintoyant, D. Lois-
nard, N. Rupin, J.-B. Marijon, O. Ulrich, M. Bornert, J.-S. Micha,
410 O. Robach, O. Castelnau, On the Accuracy of Elastic Strain Field Mea-
surements by Laue Microdiffraction and High-Resolution EBSD: a Cross-
Validation Experiment, Experimental Mechanics 56 (3) (2016) 483–492.
`doi:10.1007/s11340-015-0114-1`.
URL `http://link.springer.com/10.1007/s11340-015-0114-1`

415 [10] T. Vermeij, E. Plancher, C. Tasan, Preventing damage and re-
deposition during focused ion beam milling: The "umbrella"
method, Ultramicroscopy 186 (Supplement C) (2018) 35 – 41.
`doi:10.1016/j.ultramic.2017.12.012`.
URL `http://www.sciencedirect.com/science/article/pii/`
420 `S0304399117304060`

[11] T. Ruggles, D. Fullwood, Estimations of bulk geometrically necessary
dislocation density using high resolution EBSD, Ultramicroscopy 133
(2013) 8–15. `doi:10.1016/j.ultramic.2013.04.011`.
URL `http://linkinghub.elsevier.com/retrieve/pii/`
425 `S0304399113001174`

[12] V. Tong, J. Jiang, A. J. Wilkinson, T. B. Britton, The effect of
pattern overlap on the accuracy of high resolution electron backscat-
ter diffraction measurements, Ultramicroscopy 155 (2015) 62–73.
`doi:10.1016/j.ultramic.2015.04.019`.
430 URL `http://linkinghub.elsevier.com/retrieve/pii/`
`S0304399115001035`

[13] S. Villert, C. Maurice, C. Wyon, R. Fortunier, Accuracy assessment of
elastic strain measurement by EBSD, Journal of microscopy 233 (2) (2009)
290–301.
435 URL `http://onlinelibrary.wiley.com/doi/10.1111/j.1365-2818.2009.03120.x/full`

[14] C. Maurice, J. H. Driver, R. Fortunier, On solving the orientation gradient
dependency of high angular resolution EBSD, Ultramicroscopy 113 (2012)
171–181. `doi:10.1016/j.ultramic.2011.10.013`.
440 URL `http://linkinghub.elsevier.com/retrieve/pii/`
`S0304399111002580`

[15] T. Britton, A. Wilkinson, High resolution electron backscatter
diffraction measurements of elastic strain variations in the pres-
ence of larger lattice rotations, Ultramicroscopy 114 (2012) 82–95.
445 `doi:10.1016/j.ultramic.2012.01.004`.

16

URL   http://linkinghub.elsevier.com/retrieve/pii/
S0304399112000058

[16] C. Maurice, A. Day, R. Fortunier, High Angular Accuracy EBSD based on a 3d Hough Transform, Microscopy and Microanalysis 19 (S2) (2013) 688–689. doi:10.1017/S1431927613005436.
URL   http://www.journals.cambridge.org/abstract_
S1431927613005436

[17] J. Kacher, C. Landon, B. L. Adams, D. Fullwood, Bragg's Law diffraction simulations for electron backscatter diffraction analysis, Ultramicroscopy 109 (9) (2009) 1148–1156. doi:10.1016/j.ultramic.2009.04.007.
URL   http://linkinghub.elsevier.com/retrieve/pii/
S0304399109001132

[18] B. E. Jackson, J. J. Christensen, S. Singh, M. De Graef, D. T. Fullwood, E. R. Homer, R. H. Wagoner, Performance of dynamically simulated reference patterns for cross-correlation electron backscatter diffraction, Microscopy and Microanalysis 22 (4) (2016) 789–802.

[19] J. Alkorta, M. Marteleur, P. J. Jacques, Improved simulation based HR-EBSD procedure using image gradient based DIC techniques, Ultramicroscopy 182 (2017) 17–27. doi:10.1016/j.ultramic.2017.06.015.
URL   http://linkinghub.elsevier.com/retrieve/pii/
S0304399116301668

[20] T. Britton, C. Maurice, R. Fortunier, J. Driver, A. Day, G. Meaden, D. Dingley, K. Mingard, A. Wilkinson, Factors affecting the accuracy of high resolution electron backscatter diffraction when using simulated patterns, Ultramicroscopy 110 (12) (2010) 1443–1453. doi:10.1016/j.ultramic.2010.08.001.
URL   http://linkinghub.elsevier.com/retrieve/pii/
S0304399110002214

[21] K. Mingard, A. Day, C. Maurice, P. Quested, Towards high accuracy calibration of electron backscatter diffraction systems, Ultramicroscopy 111 (5) (2011) 320–329. doi:10.1016/j.ultramic.2011.01.012.
URL   http://linkinghub.elsevier.com/retrieve/pii/
S0304399111000271

[22] J. Alkorta, Limits of simulation based high resolution EBSD, Ultramicroscopy 131 (2013) 33–38. doi:10.1016/j.ultramic.2013.03.020.
URL   http://linkinghub.elsevier.com/retrieve/pii/
S0304399113000909

[23] T. Britton, J. Jiang, R. Clough, E. Tarleton, A. Kirkland, A. Wilkinson, Assessing the precision of strain measurements using electron backscatter diffraction ? part 1: Detector assessment, Ultramicroscopy 135 (2013) 126–135. doi:10.1016/j.ultramic.2013.08.005.

URL `http://linkinghub.elsevier.com/retrieve/pii/S0304399113002118`

[24] C. Maurice, E. Plancher, H. Klocker, A novel finite strain framework for hr-ebsd, in: Poster session of RMS EBSD Meeting, 2014. `doi:10.13140/RG.2.2.33748.81282`.
URL `https://www.researchgate.net/publication/314095375_A_novel_finite_strain_framework_for_HR-EBSD`

[25] M. A. Sutton, F. Hild, Recent advances and perspectives in digital image correlation, Experimental Mechanics 55 (1) (2015) 1–8. `doi:10.1007/s11340-015-9991-6`.

[26] J. Neggers, J. P. M. Hoefnagels, F. Hild, S. Roux, M. G. D. Geers, Direct stress-strain measurements from bulged membranes using topography image correlation, Experimental Mechanics 54 (5) (2014) 717–727. `doi:10.1007/s11340-013-9832-4`.
URL `https://doi.org/10.1007/s11340-013-9832-4`

[27] J. Kajberg, G. Lindkvist, Characterisation of materials subjected to large strains by inverse modelling based on in-plane displacement fields, International Journal of Solids and Structures 41 (13) (2004) 3439 – 3459. `doi:https://doi.org/10.1016/j.ijsolstr.2004.02.021`.
URL `http://www.sciencedirect.com/science/article/pii/S0020768304000770`

[28] H. Leclerc, J.-N. Périé, S. Roux, F. Hild, Integrated Digital Image Correlation for the Identification of Mechanical Properties, Springer Berlin Heidelberg, Berlin, Heidelberg, 2009, pp. 161–171. `doi:10.1007/978-3-642-01811-4_15`.
URL `https://doi.org/10.1007/978-3-642-01811-4_15`

[29] J. Réthoré, A fully integrated noise robust strategy for the identification of constitutive laws from digital images, International Journal for Numerical Methods in Engineering 84 (6) (2010) 631–660. `doi:10.1002/nme.2908`.
URL `http://dx.doi.org/10.1002/nme.2908`

[30] J. Neggers, J. P. M. Hoefnagels, M. G. D. Geers, F. Hild, S. Roux, Time-resolved integrated digital image correlation, International Journal for Numerical Methods in Engineering 103 (3) (2015) 157–182. `doi:10.1002/nme.4882`.
URL `http://doi.wiley.com/10.1002/nme.4882`

[31] S. Maraghechi, J. P. Hoefnagels, R. H. Peerlings, M. G. Geers, Correction of scan line shift artifacts in scanning electron microscopy: An extended digital image correlation framework, Ultramicroscopy 187 (2018) 144 – 163. `doi:https://doi.org/10.1016/j.ultramic.2018.01.002`.
URL `http://www.sciencedirect.com/science/article/pii/S0304399117300918`

18

[32] A. P. Ruybalid, J. P. M. Hoefnagels, O. van der Sluis, M. G. D. Geers, Comparison of the identification performance of conventional FEM updating and integrated DIC: COMPARISON OF THE PERFORMANCE OF FEMU AND IDIC, International Journal for Numerical Methods in Engineering 106 (4) (2016) 298–320. `doi:10.1002/nme.5127`.
URL `http://doi.wiley.com/10.1002/nme.5127`

[33] J. Neggers, B. Blaysat, J. P. M. Hoefnagels, M. G. D. Geers, On image gradients in digital image correlation, International Journal for Numerical Methods in Engineering 105 (4) (2016) 243–260, nme.4971. `doi:10.1002/nme.4971`.
URL `http://dx.doi.org/10.1002/nme.4971`

[34] P. G. Callahan, M. De Graef, Dynamical electron backscatter diffraction patterns. part i: Pattern simulations, Microscopy and Microanalysis 19 (5) (2013) 1255–1265. `doi:10.1017/S1431927613001840`.

[35] J. Neggers, Ductile interfaces in stretchable electronics : multi-scale mechanics and inverse methods, Ph.D. thesis, Eindhoven University of Technology (2013).

[36] A. Winkelmann, C. Trager-Cowan, F. Sweeney, A. P. Day, P. Parbrook, Many-beam dynamical simulation of electron backscatter diffraction patterns, Ultramicroscopy 107 (4) (2007) 414 – 421. `doi:https://doi.org/10.1016/j.ultramic.2006.10.006`.
URL `http://www.sciencedirect.com/science/article/pii/S0304399106001975`

[37] P. Chekhonin, J. Engelmann, C.-G. Oertel, B. Holzapfel, W. Skrotzki, Relative angular precision in electron backscatter diffraction: A comparison between cross correlation and hough transform based analysis, Crystal Research and Technology 49 (6) (2014) 435–439. `doi:10.1002/crat.201400075`.
URL `http://dx.doi.org/10.1002/crat.201400075`

[38] B. Blaysat, M. Grédiac, F. Sur, On the propagation of camera sensor noise to displacement maps obtained by dic - an experimental study, Experimental Mechanics 56 (6) (2016) 919–944. `doi:10.1007/s11340-016-0130-9`.
URL `https://doi.org/10.1007/s11340-016-0130-9`

[39] L. T. Hansen, B. E. Jackson, D. T. Fullwood, S. I. Wright, M. De Graef, E. R. Homer, R. H. Wagoner, Influence of noise-generating factors on cross-correlation electron backscatter diffraction (ebsd) measurement of geometrically necessary dislocations (gnds), Microscopy and Microanalysis 23 (3) (2017) 460–471.

[40] A. Ruybalid, J. Hoefnagels, O. van der Sluis, M. Geers, Image-based interface characterization with a restricted microscopic field of view, International Journal of Solids and Structures 132 (2018) 218–231.

[41] B. Blaysat, J. P. Hoefnagels, G. Lubineau, M. Alfano, M. G. Geers, Interface debonding characterization by image correlation integrated with double cantilever beam kinematics, International Journal of Solids and Structures 55 (2015) 79–91.